NSF GRANT # 0529361
NSF PROGRAM NAME: Manufacturing Enterprise Systems

Fundamental Study on Metal Embedded Micro Photonic Sensors

Xiaochun Li
University of Wisconsin-Madison

David Dornfeld
University of California, Berkeley

Brian Thomas
University of Illinois, Urbana-Champaign

Chee Wei Wong
Columbia University

Abstract: Recent developments in integrated microphotonics have led to unprecedented potential towards robust sensor enhancements for manufacturing systems. These micron-sized subwavelength structured photonic sensors could allow critical thermo-mechanical phenomena in manufacturing processes to be monitored while offering immunity to electromagnetic interference, resistance to hostile environments, multiplexing capabilities, and high rates of data collection. To implement these novel sensors into real manufacturing processes, the micro photonic sensors can be embedded at critical locations in metallic structures, which are heavily used in hostile manufacturing environments. This paper presents the study of design, fabrication, and characterization of integrated microring sensors. Various thin film optical materials were studied and single ring resonators were designed. A new approach to fabricate metal embedded microring sensors was developed. Metal embedded optical microring temperature sensors were characterized. The Q factor of the metal embedded microring sensors was measured to be around 2000, while the free spectral range (FSR) was about 5.2 nm. The temperature sensitivity of the metal embedded microring sensor was 24.2 pm/^{o}C.

1. Introduction: Thermo-mechanical phenomena monitoring is crucial in various manufacturing process. The current sensors used in metal structures (e.g. tooling) are normally large in size and are either attached to the surface where they might be far from critical locations to avoid interference with the operation of the machine, or destructively inserted into the critical locations through appropriate channels in the tooling. This makes it difficult to provide measurements with a high spatial and temporal resolution at distributed critical locations.

Micron-sized subwavelength structured photonic sensors could allow critical thermo-mechanical phenomena in manufacturing processes to be monitored, while offering opportunities for fundamental understanding and better control of manufacturing processes. Owing to their small sizes, distributed microphotonic sensors could be incorporated into mechanical structures without interfering with their normal operation. The small size of these sensors enables them to respond to environmental changes (thermal, strain and vibrational) much more quickly than ordinary macro-sensors. Moreover, they permit data to be obtained with greatly enhanced spatial resolution and sensitivity.

Significant advances in photonic device microfabrication has occurred in recent years, and has made it possible to construct very small microring resonators in a variety of materials, including glass [1], polymers [2], silicon [3], silicon nitride [4], silicon oxynitride [5], and III-V semiconductors [6]. To implement these novel sensors into real manufacturing processes, the microring sensors must survive hostile environments and provide high accuracy, long-term stability, and good reliability during service. To achieve this goal, distributed microring sensors can be embedded at critical locations, thus avoiding direct exposure from external manufacturing environments (e.g. chemicals, moisture, and contamination etc.) but without interfering with normal operation of the structure. The small size of these sensors will permit data to be obtained with significantly enhanced spatial and temporal resolution as well as superior sensitivity. Challenges for microring sensor embedding arise from the fact that most structures used in hostile manufacturing environments are metallic. It is necessary to fabricate and embed micro photonic sensors into metal structures before the sensors can be tested in manufacturing environments. SiO_2-based Fiber Bragg Grating (FBG) sensors have been successfully embedded into nickel and stainless steel for temperature and strain measurements in laser-based manufacturing processes [7]. Moreover, micro optical thin films are expected to demonstrate superior properties when compared to their macro optic counterparts, e.g. amorphous micro/nano SiO_2 and Si_3N_4 thin films have significantly higher strain limit (3~10%) than that of most metals (0.2~1%) [8]. Thus, it is promising to fabricate metal embedded microphotonic sensors that potentially can withstand the hostile manufacturing environments.

The purpose of this paper is to design microring resonators for temperature sensing, and develop an effective batch fabrication technology for microring sensors embedding in metal.

2. Sensor Principle:

Ring resonators are widely used in optical communication as wavelength-division multiplexing (WDM) add/drop filters [9]. A ring resonator system may be composed of one or two bus waveguides and a ring placed very close to them. When a light beam with a range of wavelengths is shot into the straight waveguide, the light with resonant wavelength will resonate in the ring cavity, which can further be coupled to another straight waveguide, as shown in Fig. 1.

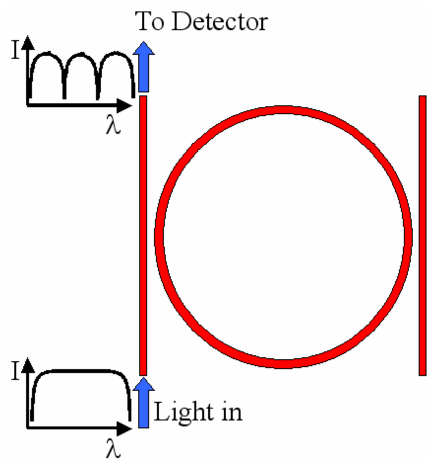

Fig. 1 Transmission spectrum of an optical waveguide coupled to a ring resonator

The resonant wavelength of a microring resonator can be expressed as [10]:

$$\lambda_o = \frac{2\pi R n_{eff}}{m} \tag{1}$$

Where R is the radius of the ring, n_{eff} is the effective refractive index of the ring and m is an integer. When thermal loads are applied to the ring, due to photothermal effects and thermal expansion, n_{eff} and R will change so that the resonant wavelengths (i.e. the dropped ones in Fig. 1 after passing through the ring resonator) will also change. By tracking the wavelength shifts, temperatures can be measured.

By differentiating Eq. (1), the resonant wavelength shift $\Delta\lambda$ is given by:

$$\Delta\lambda = \frac{2\pi}{m}\left(n_{eff}\Delta R + R\Delta n_{eff}\right) \tag{2}$$

Thus, the temperature dependence of resonant wavelength shift is related to the changes of effective refractive index and thermal expansion through the equation:

$$\frac{\Delta\lambda}{\lambda} = \left[\alpha + \frac{1}{n_{eff}}\left(\frac{dn}{dT}\right)\right]\Delta T \tag{3}$$

Where α is the effective coefficient of linear thermal expansion of the sensor material, and dn/dT is the photothermal coefficient expressing dependence of the effective refractive index on temperature. For a given signal-to-noise limit in tracking motion of a Lorentzian peak, therefore, the resolution of microring sensors to external temperature perturbation is identified by Q ($=\lambda_o/\delta\lambda$), the ratio of the resonator operating wavelength λ_o to the resonator full-width half-maximum (FWHM) $\delta\lambda$. For example, if one assumes a 3-dB differentiation limit between two overlapping Lorentzian peaks, the resolution in temperature detection is proportional to $\delta\lambda$ or equivalent to λ_o/Q. Combining with the relation between $\Delta\lambda$ and temperature, as shown in Eq. (2), this gives a temperature resolution proportional to 1/Q, that is, a larger Q gives a better temperature resolution. For microring resonators, Q from 400 in low-index contrast material systems [11] up to even 57,000 in high-index contrast silicon material systems [12] has been reported.

3. Material Selection and Sensor Design:

3.1 Material Selection: Generally, a passive photonic device consists of two types of photonic materials with a certain reflective index (n) contrast. The lower n material is used as cladding, and the one with higher n is used as the core for guiding light.

In this study silicon dioxide, which is widely used as a cladding material for optical fibers, was selected to serve as the cladding material for our ring resonators. Silicon nitride/silicon oxynitride was selected as the core material. It should be noted that the reflective index of silicon nitride/ silicon oxynitride deposited by Plasma enhanced chemical vapor deposition (PECVD) could be tuned by using different gas flow rates and different gas mixtures. With various process conditions, as listed in Table 1, the refractive index varies from pure silicon dioxide to silicon-rich silicon nitride, as shown in Fig. 2.

Table 1 PECVD Process Conditions

Material	SiH_4	NH_3	N_2	NO_2
1.Si_xN_y	10sccm	4sccm	1000sccm	-
2.Si_xN_y	8sccm	4sccm	1000sccm	-
3.SiO_xN_y	10sccm	4sccm	-	800sccm
4.SiO_2	8.8sccm	-	-	1200sccm

Base pressure: 0.5mTorr. Deposition temperature: 300°C. Power: 50W

Table 2 Sellmeier coefficients for Si_xN_y and SiO_2

Material	B_1	B_2	B_3	C_1	C_2	C_3
Si_xN_y	1.0905	1.1179	0.5921	6.1683×10^5	6.1683×10^5	-3.1077×10^5
SiO_2	0.3813	0.3841	0.2768	2.9331×10^4	2.9331×10^4	-5.5520×10^4

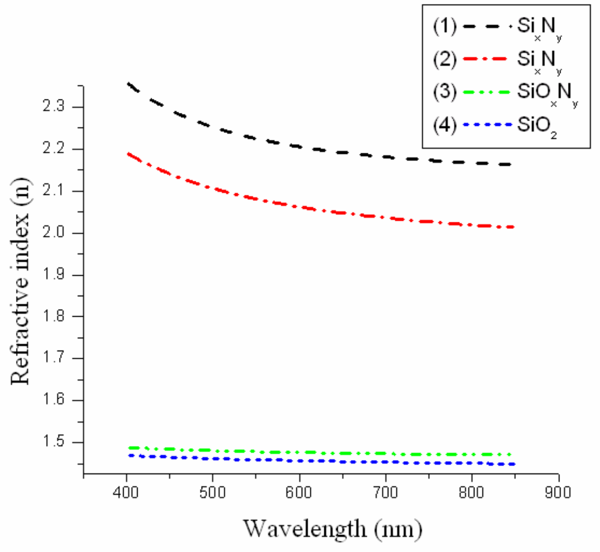

Fig. 2 Refractive index varied with various wavelengths and process conditions

Filmetrics F-20 optical reflectometer was used to measure refractive indices of the silicon dioxide and silicon nitride films. However, it can only measure the refractive indices at the wavelength range from 400 nm up to 850 nm. Since the sensor working wavelength was designed in the infrared (IR) range, Sellmeier equation [13, 14], which is an empirical relationship between refractive index and wavelength for transparent medium, was applied to estimate the refractive index in the IR range. The form of the third order Sellmeier equation is:

$$n^2(\lambda) = 1 + \frac{B_1\lambda^2}{\lambda^2 - C_1} + \frac{B_2\lambda^2}{\lambda^2 - C_2} + \frac{B_3\lambda^2}{\lambda^2 - C_3} \qquad (4)$$

Where $B_{1,2,3}$ and $C_{1,2,3}$ are experimentally determined Sellmeier coefficients. Based on the measured data points, Sellmeier coefficients for Si rich Si_xN_y and SiO_2, the materials for sensor fabrication, were derived and listed in Table 2. According to Eq. (4) and the coefficients, refractive indices of Si_xN_y and SiO_2 in the IR range can be estimated.

Nickel was selected as the substrate material due to its capability to function well in hostile environments. It has a high melting point, up to 1455 °C, and a good corrosion resistance to acids, alkalis and oxidizing agents. Furthermore, nickel offers good mechanical properties, especially good ductility [15]. It can be easily deposited by electroplating at a high rate at room temperature.

3.2 Sensor Design: The metal embedded waveguide structure is illustrated in Fig. 3. The basic limitation to the resonator, and therefore to the waveguide design, was the need to propagate light in a small radius of curvature with a minimum loss, and to ensure a single mode propagation. Therefore the thickness of top and bottom SiO_2 was chosen as 3 µm to minimize the light loss. The height of the core (Si_xN_y) was designed as 0.5 µm, so that the light could be vertically confined in the waveguide well.

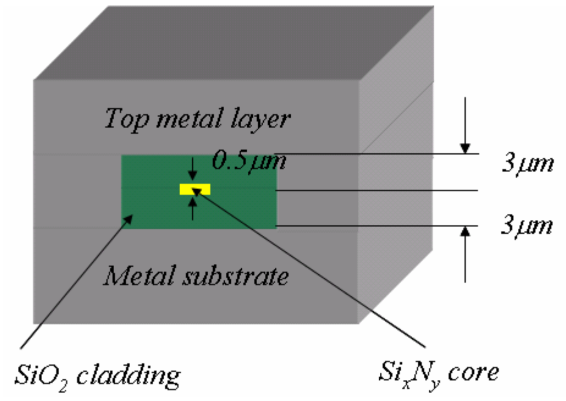

Fig. 3 Metal embedded photonic waveguide

To decide the width of the waveguide core, RSoft – FullWave (a finite-difference time-domain solver of Maxwell's equations) was applied for waveguide simulation. As shown in Fig. 4, the waveguide behaves in single mode with little leakage to the top and bottom metals when the width of the waveguide core is 1 µm, and thus, light is very well confined in the core area.

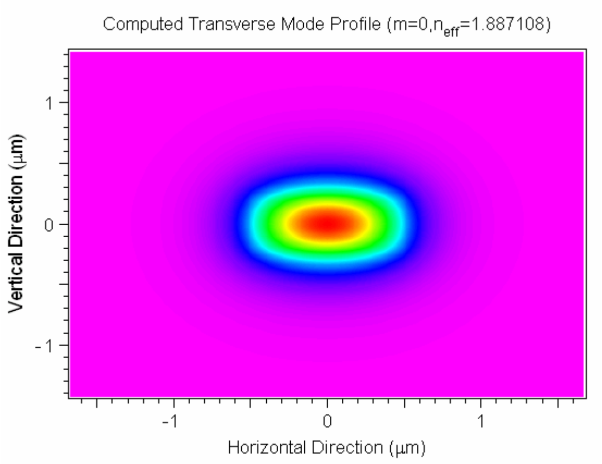

Fig. 4 Simulation of waveguide

Since the waveguide size was only 1 µm, a taper was introduced to facilitate a later input optical fiber alignment and increase the alignment tolerance. The wider waveguide size was designed to be 10 µm, and its taper length was determined by a parametric study using RSoft – FullWave. The length of the taper was scanned from 10 µm to 100 µm, and finally was set as 45 µm, at which the loss was around 10% only, as shown in Fig. 5.

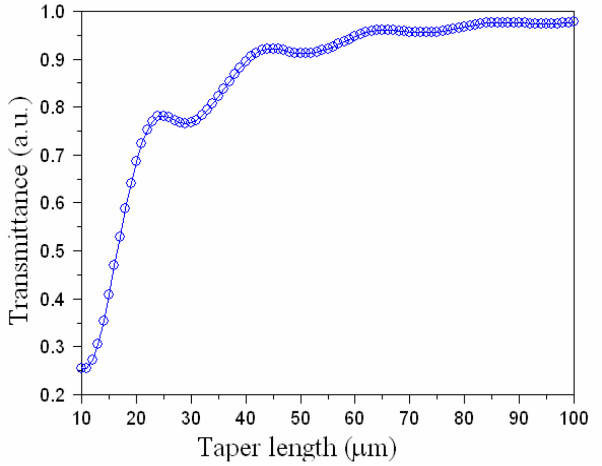

Fig. 5 Parametric study of taper length

To minimize the bending loss of the ring, a model based on effective index method [16] was employed to design the ring radius. Figure 6 illustrates the simulation results. A radius of 30 µm was chosen to guarantee minimal bending loss.

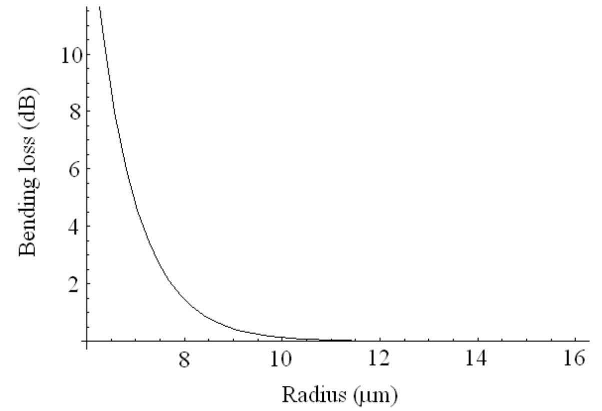

Fig. 6 Simulation of bending loss

A 200nm coupling gap was used so that light can be coupled between the straight waveguide and the ring more efficiently. Figure 7 demonstrates the layout of a microring sensor.

4. Sensor Fabrication: In this study, based on standard microfabrication and electroplating techniques, a batch of microring sensors was fabricated on an electroplated metal wafer and then embedded. Details of the fabrication are depicted in Fig. 8 and will be described below.

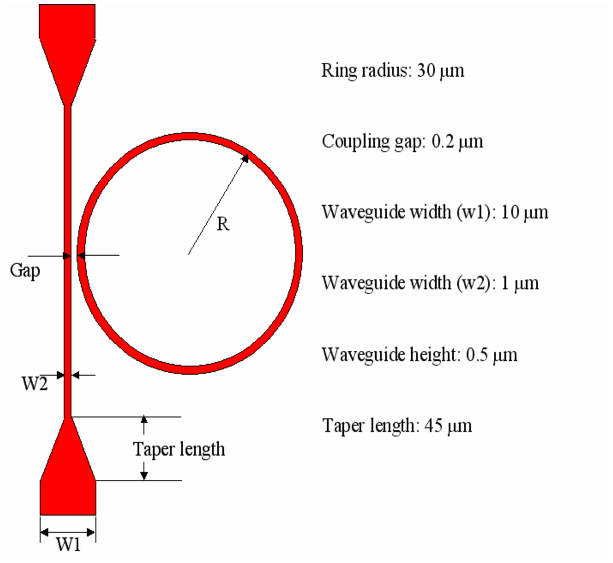

Fig. 7 Dimensions for ring resonators

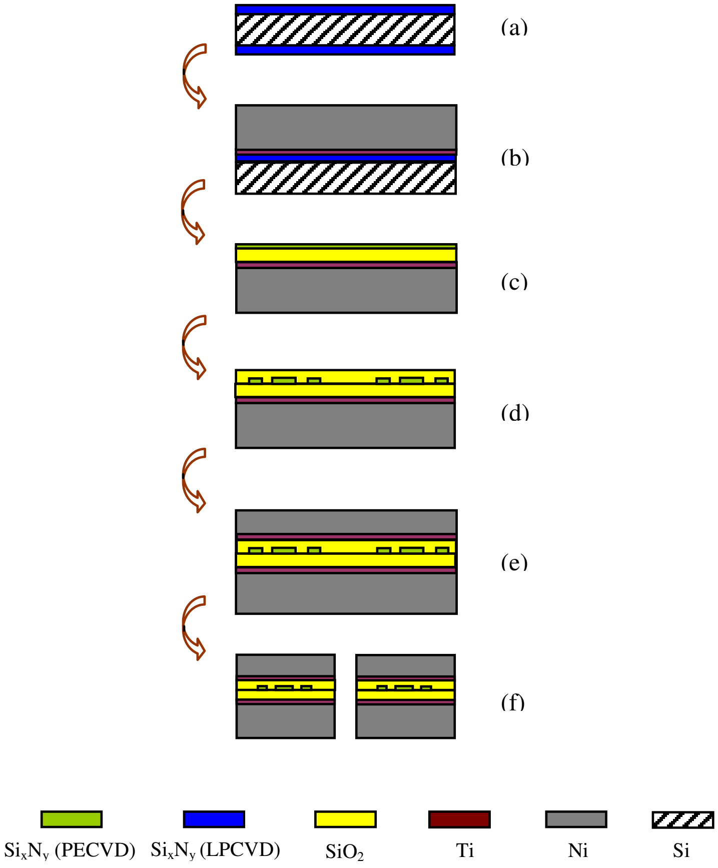

Fig. 8 Sensor fabrication process flow
a) Deposit Si_xN_y by LPCVD on Si, b) Sputter Ti/Ni followed by Ni electroplating then etch out the backside Si_xN_y, c) Deposit SiO_2 and Si_xN_y by PECVD on metal wafer, d) Employ hybrid lithography and RIE to define sensor structures, deposit top SiO_2 by PECVD, e) Sputter Ti/Ni and electroplate Ni again to embed sensors f) Dicing sensors into single units

. A 3-inch silicon wafer was first thoroughly cleaned by pre-furnace cleaning. Then a thin layer of low stress silicon nitride (0.5 µm thick) was deposited by low-pressure chemical vapor deposition (LPCVD) to serve as an etch stop layer for the subsequent KOH etching of the silicon wafer. A thin layer of Ti (50 nm) was then sputtered as an adhesion-promoting layer, followed by a Ni seed layer (300 nm). The structure was then electroplated to create a nickel substrate (approximately 220 µm) on one side. After electro-deposition of Ni, the silicon nitride (deposited by LPCVD) on the backside of the silicon wafer was etched out by reactive ion etching (RIE), and the silicon wafer was completely etched out in a 30% KOH solution at 80 ºC. The other silicon nitride layer was removed by RIE to form the metal wafer.

On the top surface of the metal wafer, a 3 µm thick silicon dioxide layer followed by a 0.5 µm thick silicon nitride layer were deposited by PECVD. Figure 8(c) shows the structure at this stage.

Since the gap between the waveguide core and coupling is only 200nm wide, electron beam (e-beam) lithography was used for patterning. Hence a hybrid lithography technique (i.e. photo/e-beam lithography combination) was applied for the sensor fabrication. S1813 with LOR 3A was patterned by optical lithography for lift-off. Thin films of Cr/Au (5/50 nm) were evaporated and followed by lift-off process to obtain etching mask and alignment marks for the e-beam lithography. Co-polymer (MMA) and PMMA bi-layers were spin coated, followed by e-beam lithography, and then Cr/Au thin films were evaporated on the top again. After lift-off, RIE with CF_4 plasma was used to etch the silicon nitride. Figure 9 is the scanning electron microscopy (SEM) image of the fabricated microring at this step. Upon the complete removal of Cr/Au films, a 3 µm thick silicon dioxide layer was again deposited by PECVD to clad the waveguide core. Figure 8(d) indicates the sensors on a metal wafer.

To embed these microring sensors into nickel, more fabrication steps were needed. Ti/Ni layers were again sputtered, and a thick nickel layer (e.g. around 70µm in this study) was electroplated to embed sensors. Figure 8(e) shows the Ni embedded optical sensors. Each single metal embedded sensor unit can be further diced out from the metal wafer using laser cutting or diamond saw dicing.

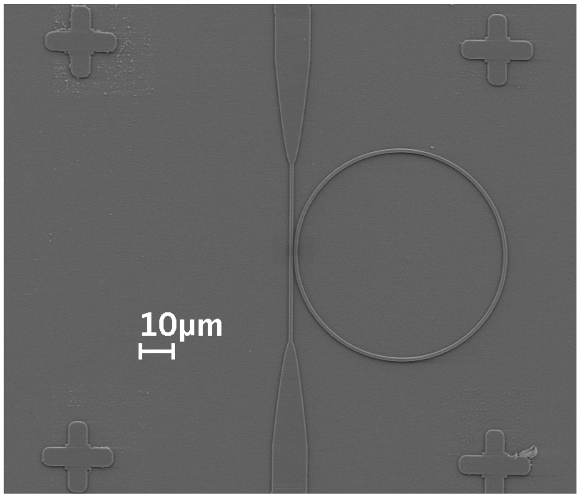

Fig. 9 SEM image of optical microring

5. Experiments and Results: To investigate the functionality of the metal embedded photonic structures, metal embedded optical waveguides, which are the basic elements of the optical sensors, were first tested. Figure 10 shows the waveguides before and after embedding. The embedded structures were mounted in epoxy followed by polishing ended with colloidal silica (50 nm). Figure 11 illustrates the polished facet of metal embedded waveguides, and the pattern of the output light.

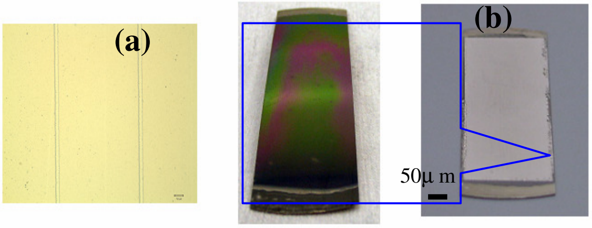

Fig. 10 (a) Waveguides before embedding, (b) Metal embedded waveguides

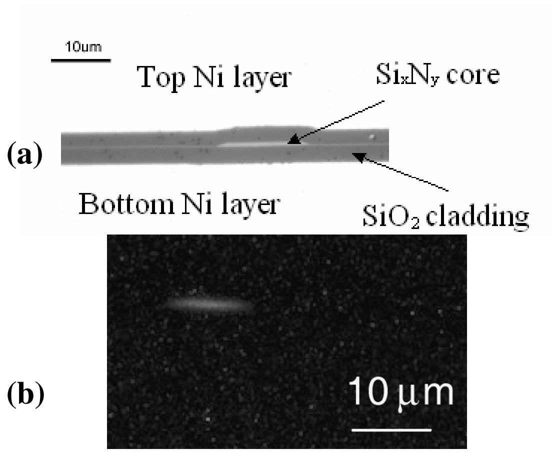

Fig. 11 (a) Polished embedded waveguide facet, (b) Output light pattern

After fabrication of sensors on metal substrate, they were selectively electroplated to embed the sensing part (microrings), so that the waveguide can be exposed for a better light coupling. Focused ion beam (FIB) was used to polish the sensor facets for light coupling and to mill a slot for fiber insertion. Figure 12 shows an example of FIB machined sensor and its polished facet.

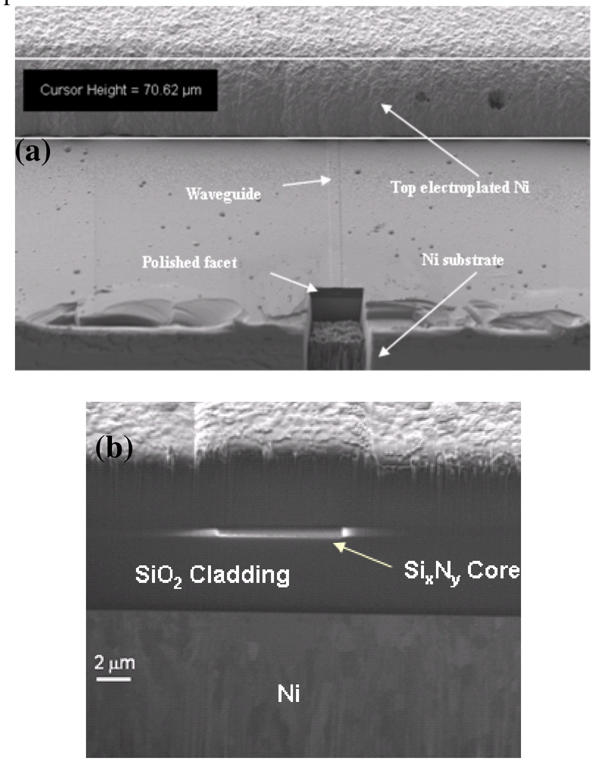

Fig. 12 (a) FIB machined embedded sensor, (b) Polished waveguide facet

The characterization was conducted using the experimental setup illustrated in Fig. 13. The FIB machined sample was fixed on a micro-stage. Tapered pigtailed fibers with a tip diameter of 2 μm were obtained by HF etching [17]. The tapered fibers were attached on the micro-stage by fiber holders. An AHURA Corporation superluminescent LED (SPOA-B35-1410-100-B14) was used as the input light source. The output light was collected by a tapered fiber tip and connected to an Agilent 86142B optical spectrum analyzer (OSA). A soldering iron tip was placed near to the sample to serve as a tunable heat source and two K-type wire thermocouples were attached near to the ring to provide the actual temperature.

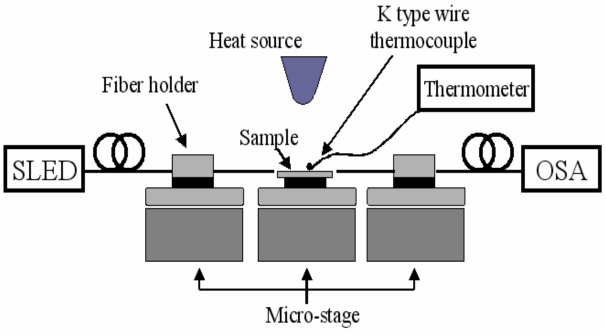

Fig. 13 Experimental setup for characterization

Figure 14 shows the measured spectral response (normalized to its maximum) for the microring resonator at room temperature (25.5 °C). The measurements indicate the Q factor of the resonator is around 2000, and FSR is about 5.2 nm. It should be note that the fluctuation in transmittance could be introduced by the misalignment caused by fiber vibration.

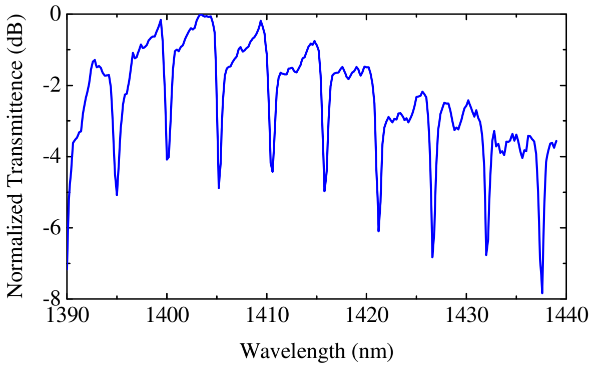

Fig. 14 Measured spectral response (normalized to maximum) at room temperature

Resonant wavelength shift with temperature is shown in Fig. 15. Lorentz fitting was employed to determine the shift in resonance. As the temperature rose from 25.5°C to 88°C, the resonant peak shifts from 1405.29nm to 1406.81nm. Figure 16 illustrates the relationship between resonant wavelength and temperature. The linear fitting equation shows the temperature sensitivity of the device is 24.2 pm/°C.

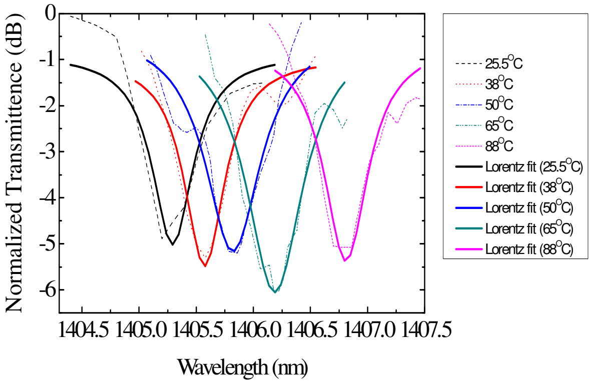

Fig. 15 Spectral response (normalized to maximum) with respect to temperature

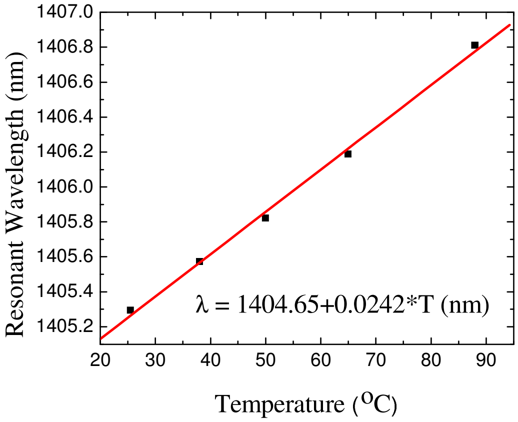

Fig. 16 Resonant wavelength as a function of temperature

Theoretical temperature sensitivity can be estimated by Eq. (3). With the assumptions of a constant coefficient of thermal expansion (CTE) for nickel, and a perfect bonding between the optical thin films and electroplated nickel, the temperature sensitivity was calculated to be 23.6 pm/°C. The theoretical sensitivity was about 3% smaller than that from experiments. The difference might be attributed to errors in the estimated refractive index n_{eff}, 1.887, the constant CTE of nickel, 12 με/°C, and dn_{eff}/dT, $9.1*10^{-6}$/°C [18]. It is especially difficult to obtain an accurate value of dn_{eff}/dT (since it is a processing dependent value) and the CTE mismatch between silica and silicon nitride could also introduce some errors on dn_{eff}/dT.

6. Summary:

Integrated microphotonics, when used as micro sensors, have a great potential for numerous manufacturing applications. These micron-sized photonic sensors could allow critical thermo-mechanical phenomena in manufacturing processes to be monitored, while offering immunity to electromagnetic interference, resistance to hostile environments, multiplexing capabilities, and high rates of data collection. This paper studied optical microring sensors that offer new opportunities for fundamental understanding and better control of emerging meso/micro manufacturing processes.

Optical properties of various thin film materials were studied for metal embedded microring sensors. Single mode waveguides and ring resonators were designed. A process to fabricate metal embedded photonic sensors based on standard microfabrication and electroplating techniques was developed. Metal embedded optical microring sensors were fabricated and characterized. The Q factor of the metal embedded microring is around 2000 and FSR is about 5.2 nm. The temperature sensitivity of the embedded microring sensor is about 24.2pm/°C.

7. Acknowledgments:

This work is supported by the National Science Foundation under Grant # 0529361

8. REFERENCE:

[1] Chu, S. T., Little, B., Pan, W., Kaneko, T., Sato, S. and Kokubun, Y., 1999, “An 8 Channel Add/Drop Filter Using Vertically Coupled Microring Resonators Over a Cross Grid,” IEEE Photon. Technol. Lett., **11**, pp. 691-693

[2] Rabiei, P. and Steier, W.H., 2002, “Polymer Micro-ring Filters and Modulators,” J. of Lightwave Technol., **20**, pp. 1968-1975,

[3] Little, B. E., Foresi, J. S., Steinmeyer, G., Thoen, E. R., Chu, S. T., Haus, H. A., Ippen, E. P., Kimerling, L. C. and Greene, W., 1998, “Ultra-compact Si-SiO_2 Microring Resonator Optical Channel Dropping Filters,” Photonics Technol. Lett., **10**, pp. 549-551

[4] Klunder, D. J. W., Krioukov, E., Tan, F. S., van der Veen, T., Bulthuis, H. F., Sengo, G., Otto, C., Hoekstra, H. J. W. M. and Driessen, A., 2001, “Vertically and Laterally Waveguide-coupled Cylindrical Microresonators in Si_3N_4 on SiO_2 Technology,” Appl. Phys. B, **73**, pp.603-608

[5] Lee H.-P., Park J.-J., Ryoo H.-H., Gol Lee S., Beom Hoan O. and Lee E.-H., 2003, "Resonance Characteristics of Waveguide-coupled Polyimide Microring Resonator," Opt. Materials, **21**, pp.535 - 541

[6] Rafizadeh, D., Zhang, J. P., Hagness, S. C., Taflove, A., Stair, K. A., Ho, S. T. and Tiberio, R. C., 1997, "Waveguide-coupled AlGaAs/GaAs Microcavity Ring and Disk Resonators with High Finesse and 21.6 nm Free Spectral Range," Opt. Lett., **22**, pp.1244-1246

[7] Li, X., 2001, "Embedded Sensors in Layered Manufacturing," Ph.D. thesis, Stanford University, USA

[8] Halg, B., 1990, "On a Nonvolatile Memory Cell Based on Micro-Electro-Mechanics," Electro Mechanical Systems Workshop, Napa Valley, California, pp.172-176

[9] Choi, J. M., Lee, R. K. and Yariv, A., 2001, "Control of Critical Coupling in a Ring Resonator-fiber Configuration: Application to Wavelength-selective Switching, Modulation, Amplification, and Oscillation", Opt. Lett., **26**, pp. 1236-1238

[10] Okamoto, K., 2000, Fundamentals of Optical Waveguides, Academic Press, San Diego, California, USA, Chap. 4.

[11] Sherwood, T., Young, A. C., Takayesu, J., Jen, A.K.Y., Dalton, L.R. and Chen A., 2005, "Microring Resonators on Side-Polished Optical Fiber," Photonics Technol. Lett., **17**, pp. 2107-2109

[12] Baehr-Jones, T., Hochberg, M., Walker, C and Scherer, A., 2004, "High-Q Ring Resonators in Thin Silicon-on-insulator," Appl. Phys. Lett. **85**, pp. 3346-3347

[13] Modreanu, M., Gartner, M., Tomozeiu, N. and Szekeres, A., 2001, "Optical and Electrical Properties of As Deposited LPCVD SiO_xN_y Thin Films," J. Optoelectron. Adv. Mater., **3**(2), pp. 275-285

[14] Warnecke, A. J. and LoPresti, P. J., 1973, "Refractive Index Dispersion in Semiconductor-related Thin Films," IBM J. Res. Develop, **17**(3), pp. 256-262

[15] Lou, J., Allameh, S., Buccheit, T. and Soboyejo, W. O., 2003, "An investigation of the effects of thickness on mechanical properties of LIGA nickel MEMS structures," J. Materials Sci. **38**, pp. 4129-4135

[16] Subramaniam, V., De Brabander, G.N., Naghski, D.H. and Boyd, J.T., 1997, "Measurement of Mode Field Profiles and Bending and Transition Losses in Curved Optical Channel Waveguides," IEEE J. Lightwave Technol., **15**, pp. 990-997

[17] Alder, T., Stohr, A., Heinzelmann, R. and Jager, D., 2000, "High-Efficiency Fiber-to-Chip Coupling Using Low-Loss Tapered Single-Mode Fiber," IEEE Photonics Thechnol. Lett., **12**, pp.1016-1018

[18] Li, X., Prinz, F. and Seim, J., 2001, "Thermal Behavior of a Metal Embedded Fiber Bragg Grating Sensor," Smart Mater. Struct., **10**, pp.575-579